Charge-State Dependent Vibrational Relaxation in a Single-Molecule Junction

Xinya Bian,[1] Zhixin Chen,[1] Jakub K. Sowa,[2] Charalambos Evangeli,[1] Bart Limburg,[3] Jacob L. Swett,[1] Jonathan Baugh,[4] G. Andrew D. Briggs,[1] Harry L. Anderson,[3] Jan A. Mol,[5] and James O. Thomas[1,*]

[1]*Department of Materials, University of Oxford, Oxford OX1 3PH, United Kingdom*
[2]*Department of Chemistry, Rice University, Houston, Texas 77005, USA*
[3]*Department of Chemistry, University of Oxford, Oxford OX1 3TA, United Kingdom*
[4]*Institute for Quantum Computing, University of Waterloo, Waterloo, Ontario N2L 3G1, Canada*
[5]*School of Physical and Chemical Sciences, Queen Mary University, London E1 4NS, United Kingdom*

(Received 15 March 2022; accepted 20 October 2022; published 9 November 2022)

The outcome of an electron-transfer process is determined by the quantum-mechanical interplay between electronic and vibrational degrees of freedom. Nonequilibrium vibrational dynamics are known to direct electron-transfer mechanisms in molecular systems; however, the structural features of a molecule that lead to certain modes being pushed out of equilibrium are not well understood. Herein, we report on electron transport through a porphyrin dimer molecule, weakly coupled to graphene electrodes, that displays sequential tunneling within the Coulomb-blockade regime. The sequential transport is initiated by current-induced phonon absorption and proceeds by rapid sequential transport via a nonequilibrium vibrational distribution of low-energy modes, likely related to torsional molecular motions. We demonstrate that this is an experimental signature of slow vibrational dissipation, and obtain a lower bound for the vibrational relaxation time of 8 ns, a value dependent on the molecular charge state.

DOI: 10.1103/PhysRevLett.129.207702

Charge transport through nanostructures, and molecules in particular, is strongly influenced by coupling between electronic and mechanical degrees of freedom [1–10]. Geometric differences between molecular charge states mean that electron-transfer steps are accompanied by vibrational transitions. In the limit of weak molecule-lead coupling, transport through such structures can be viewed as a sequence of heterogeneous electron transfers (ET) [7,11]. Heterogeneous ET is also a fundamental step in heterocatalysis, solar-energy harvesting, and organic electronics [12–14]. Conventional descriptions of this process typically assume a thermalized nuclear environment and, although it is established that nonequilibrium vibrational dynamics (induced by photoexcitation or the electron transfer itself) can have a profound impact on charge-transfer rates, studying these effects experimentally remains challenging [13–18]. In this context, single-molecule junctions offer a promising platform for investigating coupled electronic-nuclear dynamics as the ET driving force is controlled, coupling to individual modes can be resolved, and measurements can be performed in the steady-state limit.

Vibrational effects in single-molecule junctions are particularly important in the weak molecule-electrode coupling limit, as strong electron-electron interactions lead to Coulomb blockade (CB) and charge states are well defined. Transport through the molecule occurs either via resonant sequential tunneling, i.e., consecutive ET steps, outside the CB regime or via off-resonant cotunneling inside the CB regime. Like sequential tunneling, cotunneling can excite vibrations above a bias threshold through inelastic cotunneling [7]. If cotunneling-excited vibrational states relax sufficiently slowly, sequential processes originate from excited states, blurring the boundary between resonant and off-resonant tunneling regimes [19,20]. Cotunneling-assisted sequential tunneling is predicted to give distinctive features in the transport spectrum, absorption sidebands, extending into the CB regime [1,10,19,21–24]. In this Letter we report the experimental observation of such sidebands, and modeling indicates that torsional motions of the molecule are the probable origin. We calculate a vibrational dissipation rate of > 8 ns that depends on the molecular charge state and links the nonequilibrium dynamics to the molecular geometry.

The device architecture, displayed in Fig. 1, has been described previously [25]. A high-κ, 10 nm-thick, HfO_2 dielectric gives a large electrostatic coupling between molecular states and the gate potential V_g (here $\alpha_g = 0.5$ eV/V). The molecule, a fused zinc-porphyrin dimer (FP2) [Fig. 1(c)], has a small charging energy which, combined with the large gate coupling, allows multiple charge states to be studied. FP2 is synthesized by Sonogashira coupling of a dibromo- edge-fused zinc porphyrin dimer [26] with an ethynylpyrene derivative [27,28]. Pyrene groups anchor the molecule to the graphene source and drain through π stacking and provide weak molecule-electrode coupling, Γ. Electroburnt graphene nanoelectrodes can display transport features prior to

 © 2022 American Physical Society

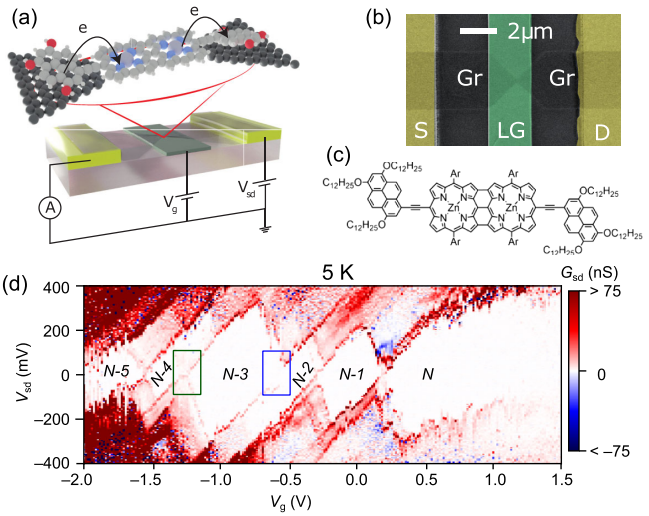

FIG. 1. (a) Device schematic. (b) False-color SEM image of graphene (Gr) transferred onto source (S) and drain (D), and local-gate electrode (LG). Gr is patterned into a bowtie shape to produce nanoelectrodes via electroburning. (c) Molecular structure of FP2, Ar: 3,5-*bis*(trihexylsilyl)phenyl. (d) Conductance map (dI_{sd}/dV_{sd}) of the FP2 device; transitions studied are outlined in green and blue.

molecular deposition, and therefore devices were measured before and after deposition to ensure we only study transport features related to FP2. From 98 devices measured at 5 K, the majority displayed resonant tunneling features prior to molecular deposition, consistent with previous work [27]. Five displayed clear resonant transport only after deposition and had consistent addition energies with the device studied in detail here. The presented device has a molecule-electrode coupling that results in relative magnitudes of the sequential tunneling, cotunneling, and relaxation rates that enable experimental observation of absorption sidebands.

A large V_g-range conductance map [Fig. 1(d)] confirms the molecule is weakly coupled to the graphene electrodes. Off-resonant transport is suppressed due to CB and multiple Coulomb diamonds, with addition energies in the range, 150–300 meV, observed and separated by resonant transport regions. Because of the electron-rich anchor groups and p doping of graphene by the substrate [29], charge states are assigned to successive oxidized states of FP2, i.e., $N-5$ to N, N being the number of electrons on the neutral molecule. The assignment and addition energies are inline with studies on the same family of molecules [9,30,31]. We focus on electron-vibration coupling features manifested in the charge transitions at $V_g = -1.25$ V, assigned to the $N-4/N-3$ transition (green box), and $V_g = -0.6$ V, assigned to $N-3/N-2$ (blue box).

Figure 2(a) displays high-resolution conductance maps of the $N-4/N-3$ transition. The solid slanted lines define the usual resonant transport region separating $N-4$ and $N-3$ diamonds. Lines of increased conductance running parallel to the diamond edges (dashed and dotted lines) are caused by additional transport channels to the ground-state or ground-state transition between $N-4$ and $N-3$. The low energy of these excited-state channels, around 9 meV, point to a vibrational origin. Vibrational transitions of similar energy were observed in porphyrin monomers [9]. Under weak coupling, resonant transport is dominated by first-order sequential tunneling processes, i.e., $|N,q\rangle$ to $|N',q'\rangle$ where $N' = N \pm 1$, and each additional channel involves either the hopping on or off ET

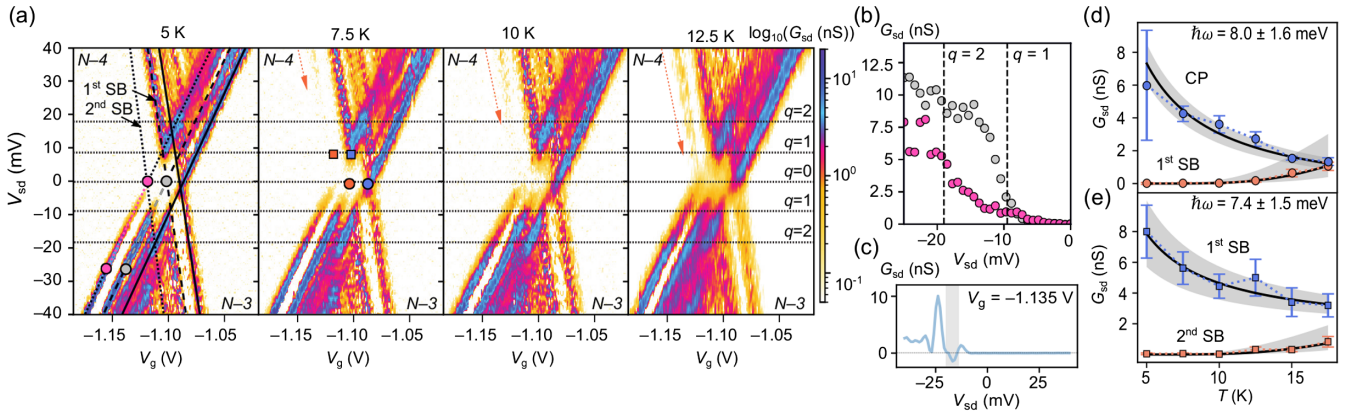

FIG. 2. (a) Temperature-dependent conductance maps of the $N-4/N-3$ transition, showing quasiperiodic resonant transport features. The onset of the second sideband is indicated (orange arrow). (b) Conductance measured along the first [between gray markers, (a)] and second (pink markers) sidebands shows suppression below $eV_{sd} < n\hbar\omega_q$. (c) Negative differential resistance (gray band) between the first two sidebands. (d) Temperature dependence of the Coulomb peak (CP) and first sideband (SB), [orange and blue circles, (a)]. The ground state shows a simple $1/T$ relationship (black line). The first sideband is suppressed, increasing due to thermal population of $q = 1$, fitted by Eq. (4) (black line). (e) Temperature-dependent conductance through the first and second sideband [square markers on (a)] at $eV_{sd} = \hbar\omega_q$; the conductance of the first sideband is high and decays as $1/T$ (black line) whilst the second grows with temperature. Error bars are from a fit to the conductance trace around the SB or CP, and gray areas are confidence bands on the fits.

steps required to transport an electron through the junction to be accompanied by a change in vibrational state, i.e., $\Delta q = q' - q \neq 0$. These steps generate out-of-equilbrium vibrational excitations in the molecule, but if vibrational relaxation is much faster than sequential ET then under steady-state conditions the system can be treated as in equilibrium. Under equilibrium and at low temperature, only the vibrational ground state is appreciably populated, CB is maintained, and sequential tunneling current should be strictly bound within the solid lines defining the ground-state to ground-state resonant tunneling transition. Here, however, more complex behavior is observed. The additional transport channels at energies of $\hbar\omega_q = 9$ meV (dashed and dotted slanted lines) do not terminate at the CB boundaries but instead extend into the $N-4$ diamond, forming sidebands to the Coulomb peak. The $N-4$ sidebands run parallel to diamond edges, indicating the current results from sequential tunneling. The first sideband corresponds to a transition with $\Delta q = -1$, and thus sequential tunneling must involve at least the first vibrationally excited state of $N-4$. For the second sideband, $\Delta q = -2$ and sequential tunneling originates from the second vibrationally excited state of $N-4$. The sidebands are present at 5 K, despite the absence of equilibrium population in $|N-4, 1\rangle$.

Figure 2(b) shows the sidebands do not cross the zero-bias axis. At 5 K conductance of the first sideband [Fig. 2(b), gray] is suppressed below $|eV_{\mathrm{sd}}| = \hbar\omega_q$, and the second sideband conductance (pink) below $2\hbar\omega_q$. This suggests that features within the $N-4$ Coulomb diamond result from cotunneling-assisted sequential tunneling [19,20]. The emergence of the first sideband is shown in Fig. 3(a). At low voltages ($|eV_{\mathrm{sd}}| < \hbar\omega_q$) cotunneling must be elastic ($q' = q$) and will contribute a small portion of tunneling current (cotunneling is second order in Γ). Above $|eV_{\mathrm{sd}}| = \hbar\omega_q$ inelastic cotunneling events, which leave the molecule in an excited vibrational state, are energetically allowed [Fig. 3(a)]. If the vibrational excitation resulting from inelastic cotunneling relaxes slowly compared with sequential tunneling rates, $W^{N,N'}_{q,q'}$, specifically $W^{N-4,N-3}_{1,0}$, then a sequential tunneling pathway to the $N-3$ ground state is opened up [Fig. 3(a)]. The $|N-3, q=0\rangle$ state can subsequently undergo sequential tunneling to up to the second vibrationally excited state of $N-4$. If electron-phonon coupling, parametrized by the constant λ_q, is weak (< 1) then the transition to $|N-4, q=0\rangle$ is most likely, and the molecule returns to the vibrational ground state until inelastic cotunneling restarts the cycle. If $\lambda_q > 1$ then transitions to $|N-4, q=1,2\rangle$ out compete the return to the $N-4$ ground state, and a single inelastic cotunneling event leads to sustained sequential tunneling through the molecule, even in the CB region, via vibrationally excited states of $N-4$. Therefore the prominence of the sidebands is enhanced with strong electron-phonon coupling.

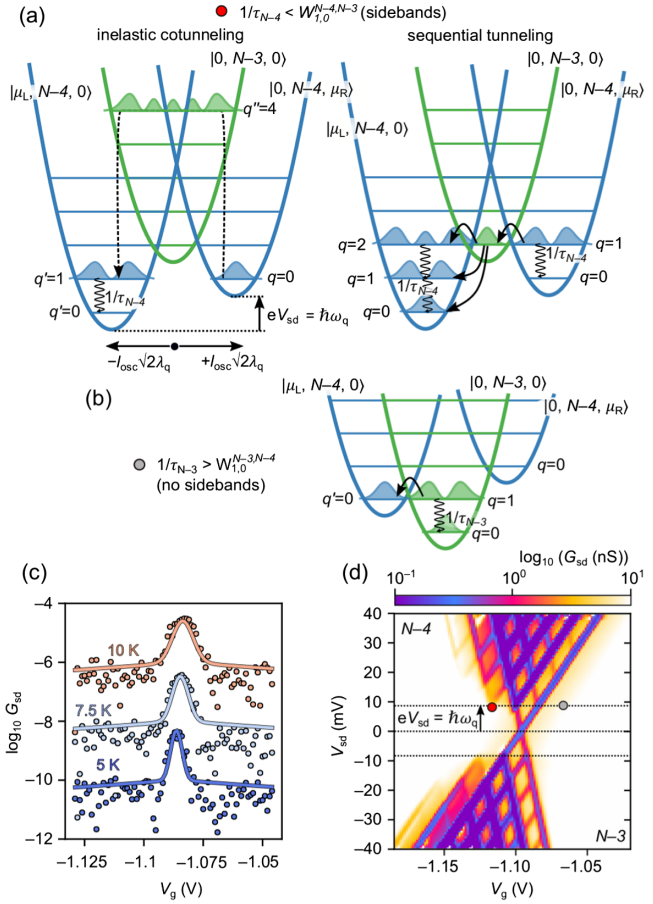

FIG. 3. (a) Onset of first sideband (red dot, panel (d)). Blue $N-4$ parabolas correspond to an electron at the Fermi level of left $|\mu_L, N-4, 0\rangle$ or right $|0, N-4, \mu_R\rangle$ electrode. The green parabola corresponds to the electron being on the molecule: $|0, N-3, 0\rangle$. $N-4$ parabola have the same x-position, but are offset from $N-3$ by $\pm l_{osc}\sqrt{2}\lambda_q$ to visualise electron flow from right to left lead. Inelastic cotunneling promotes the molecule to $q=1$. If relaxation ($1/\tau_{N-4}$) is smaller than $W^{N-4,N-3}_{1,0}$, sequential tunneling proceeds via excited states of FP2, leading to sidebands. (b) Parabolas at the onset of the first $N-3$ sideband (grey dot) are not observed as $1/\tau_{N-3}$ out-competes sequential tunneling. (c) Fits to zero-bias gate traces yield λ_q and $\bar{\Gamma}$ values, here $\lambda_q = 2.7$, $\bar{\Gamma} = 40$ μeV. Traces are offset for clarity. (d) Modelled conductance map at 5 K, using $\hbar\omega_q = 9$ meV, $\lambda_q = 2.7$, $\bar{\Gamma} = 40$ μeV, $1/\tau_{N-4} = 1/100\times W^{N-4,N-3}_{1,0}$, $1/\tau_{N-3} = 100 \times W^{N-3,N-4}_{1,0}$; sequential tunneling rates are calculated at the red and grey points respectively.

We look to a understand these mechanisms quantitatively. Conductance is a sum of cotunneling and sequential tunneling contributions: $G_{\mathrm{sd}} \approx G_{\mathrm{seq}} + G_{\mathrm{cot}}$. At low temperature and zero bias these are given analytically by [32]

$$G_{\mathrm{seq}} = -\frac{2e^2}{\hbar}\frac{\Gamma_L\Gamma_R}{\Gamma_L+\Gamma_R}\frac{f'(\epsilon_d)}{1+f(\epsilon_d)}e^{-\lambda^2} \qquad (1)$$

and

$$G_{\mathrm{cot}} = \frac{2e^2}{h}\frac{\Gamma_L\Gamma_R}{1+f(\epsilon_d)}\left[\frac{1-f(\epsilon_d)}{(\epsilon_d+\lambda^2\hbar\omega)^2}+\frac{2f(\epsilon_d)}{(\epsilon_d-\lambda^2\hbar\omega)^2}\right] \quad (2)$$

where Γ_L and Γ_R are couplings of the molecule to left or right electrodes, $f(\epsilon_d)$ is the Fermi distribution at the energy of the molecular transition (ϵ_d), and $f'(\epsilon_d)$ the derivative. We fit zero-bias conductance to $\bar{\Gamma}$ and λ_q, shown in Fig. 3(c), where $\bar{\Gamma} = \Gamma_L\Gamma_R/(\Gamma_L+\Gamma_R)$. The two parameters cannot be determined independently (they are positively covariant [28]), although we can determine a range for them. Sequential tunneling is exponentially suppressed in λ_q. However cotunneling still occurs via highly excited virtual states of $N-3$; therefore at large λ_q (> 2.8) there are significant contributions from elastic cotunneling not observed experimentally. This sets an upper bound for λ_q. Simulations (*vide infra*) of the conductance map show at $\lambda_q < 2$ ($\bar{\Gamma} < 1$ μeV) the sidebands become too low in conductance to observe. As shown by another device in the Supplemental Material [28], the absence at low $\bar{\Gamma}$ results from reduced inelastic cotunneling and sequential tunneling rates that initiate and sustain the sidebands, and low λ enhances rates of ET from excited vibrational states of $|N-3,q\rangle$ to the ground state, $|N-4,q=0\rangle$ due to larger Franck-Condon factors. Therefore, we find pairs of parameters within ranges of 2–3 for λ_q and 1–100 μeV for $\bar{\Gamma}$. Theoretical work predicted that slow vibrational relaxation coupled with λ_q values of 2–3 would result in negative differential conductance (NDC) after the conductance peaks of the sidebands, due to depopulation of the nonequilibrium vibrational distribution to the ground state by sequential transfer as the sidebands enter the bias window [23]. Our experimental observation of NDC [Fig. 2(c)] and calculated range of λ_q are consistent with this prediction. The criteria for the emergence of the first $N-4$ sideband is $1/\tau_{N-4} \leq W_{1,0}^{N-4,N-3}$. Therefore calculation of the sequential rate yields a lower bound for the vibrational relaxation time. Sequential tunneling rates are given by [32]

$$W_{q,q';a}^{N-4,N-3} = 2\Gamma_a|M_{q,q'}|^2 f_a(\epsilon+[q'-q]\hbar\omega) \quad (3)$$

where $M_{q,q'}$ are Franck-Condon matrix elements. Across the range of λ_q, $\bar{\Gamma}$, calculated values of $W_{1,0;L}^{N-4,N-3}$ vary from 56 to 120 MHz, [28] giving a lower bound of $\tau_{N-4} > 8$ ns. The absence of sidebands within the $N-3$ charge state is an intriguing part of the system dynamics. If $1/\tau_{N-3} > W_{1,0}^{N-3,N-4}$ the sidebands are not present [Fig. 3(b)] pointing to a charge-state dependence of vibrational relaxation rates. Using a minor extension to the model developed by Koch *et al.* to include this effect, we calculate the conductance map [Fig. 3(d)] using these inequalities [32], showing good correspondence with the experimental data, reproducing the key features of the transport spectrum.

Temperature dependence of the conductance supports the assignment of the features as cotunneling-assisted sidebands. At zero bias the Coulomb peak and first sideband follow equilibrium behavior [Fig. 2(d)]. The conductance of the Coulomb peak ($V_{\mathrm{CP}} = -1.08$ V) decays as $G_{\mathrm{max}} \propto (1/k_BT)$, due to thermal broadening of electrode Fermi-Dirac distributions, and the conductance where the first sideband would cross $V_{\mathrm{sd}} = 0$ [from which ET is driven from $q = 1$, orange circle, Fig. 2(a)] can be fitted to the product of thermal broadening and the Bose distribution [8]:

$$G_{\mathrm{max}} \propto \frac{1}{k_BT} \times \frac{1}{\exp(\hbar\omega_q/k_BT)-1} \quad (4)$$

with $\hbar\omega_q = 8 \pm 1$ meV. This demonstrates the zero-bias conductance increases due to increasing equilibrium population in $q = 1$. The picture differs at higher bias [Fig. 2(e)]. At $eV_{\mathrm{sd}} = \hbar\omega_q$ the conductance of the first sideband is already high at 5 K and decreases with increasing temperature, indicating a substantial nonequilibrium population at $eV_{\mathrm{sd}} = \hbar\omega_q$, that must be driven by the tunneling dynamics of the system (inelastic cotunneling and slow relaxation). For the second sideband [orange arrow, Fig. 2(a)] sequential tunneling begins from $|N-4,q=2\rangle$. At $|eV_{\mathrm{sd}}| = \hbar\omega_q$ (orange square), this state arises from two inelastic excitations of the ground state or an inelastic excitation of thermally populated $|N-4,q=1\rangle$. The latter becomes appreciable only at higher temperature. Since the emergence of the second sideband at positive bias is only observed above 10 K, this suggests the second mechanism dominates, and fitting to Eq. (4) gives $\hbar\omega_q = 7.4 \pm 1.5$ meV. The sidebands are stronger at negative bias, likely due to asymmetries in molecule-electrode coupling, common in single-molecule devices [27], and the asymmetric voltage drop across the junction ($\alpha_S = 0.24$, extracted from diamond edges).

The neighboring transition, $N-3/N-2$ [blue box, Fig. 1(d)] also displays signatures of strong electron-phonon coupling, i.e., Franck-Condon blockade involving a mode of 10 meV [28]. Vibrational modes that couple strongly to electron-transfer processes are those that displace atoms along the same vectors that define the nuclear rearrangement. Density functional theory calculations aid our understanding of strong electron-vibrational coupling in the oxidations of FP2 [33]. Frequency calculations [B3LYP/6-31G(d)] on FP2 optimized in the N to $N-4$ states show modes around 9 meV correspond to out-of-plane motions, i.e., saddling of the porphyrins, or torsional motions between pyrene-porphyrin systems. We refrain from a mode-specific assignment as a full calculation of ω_q, λ_q pairs should also account for binding to the substrate that can induce shifts in vibrational frequencies [34,35], and center-of-mass oscillations that can also couple to electron transfer [2]. However, as Fig. 4 shows, the angle between

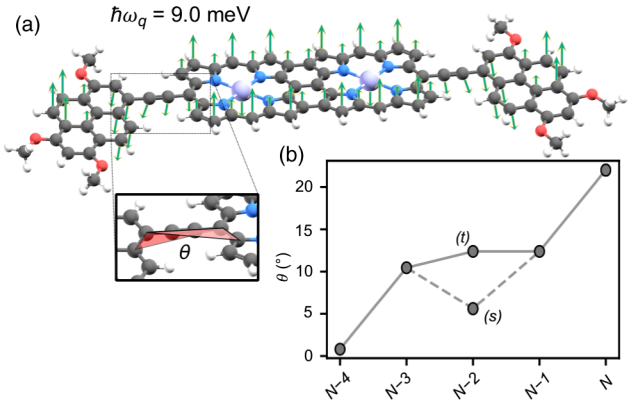

FIG. 4. (a) Example vibrational mode around 9 meV. (b) DFT-calculated dihedral angle θ [shown in (a)] in each charge state. For $N-2$, singlet and triplet (the ground state) are labeled by (s) and (t).

the π systems indeed varies with charge state. This rationalizes why a mode of torsional nature is likely to couple strongly to ET in the oxidations of FP2, and is consistent with previous observations in porphyrin monomers with pyrene anchoring groups [9].

The origins of slow vibrational relaxation are more difficult to pin down; dissipation is affected by energy-dependent coupling to the phononic background of the environment and intramolecular vibrational redistribution [36,37]. A room-temperature study of vibrational lifetimes in anthracene derivatives in molecular junctions gave values in the 10–100 picosecond range, similar to solution measurements, where picosecond relaxation is typical [38,39]. Generally, vibration relaxation slows as temperature decreases [37]. For example, our measured relaxation time of $\tau_{N-4} > 8$ ns, giving a Q factor $(\tau E/h)$ of $> 20\,000$, is comparable to that found for the radial breathing mode of a carbon nanotube at 5 K [40]. Particularly interesting is the link between the molecular charge state and, consequently, its geometry, and the relaxation rate. We note that FP2 in the $N-4$ oxidation state has a coplanar porphyrin-pyrene system (Fig. 4). Therefore the potential resulting from rotation around the angle θ is approximately harmonic (an approximation underpinning the above analysis), whereas for N to $N-3$ with nonzero values of θ the potential is quartic with two minima, corresponding to *syn* and *anti* conformations of the pyrene-porphyrin-pyrene system. Quartic potentials increase the energy density of low-energy modes and, combined with the substrate-induced asymmetry, could expedite intramolecular vibrational relaxation for the N to $N-3$ states [41,42]. Therefore, moving beyond the harmonic approximation may be required to fully unravel the tunneling dynamics at play. The observation of sidebands depends crucially on the (in our case uncontrolled) electronic and vibrational couplings between the nanoscopic system and its environment and is thus device specific; however, the uncovered principle will influence thermodynamics of ET in any quantum system.

This work was supported by the EPSRC (Grants No. EP/N017188/1 and No. EP/R029229/1). J. A. M. acknowledges funding from the Royal Academy of Engineering and a UKRI Future Leaders Fellowship, Grant No. MR/S032541/1. The authors would like to acknowledge the use of the University of Oxford Advanced Research Computing (ARC) facility in carrying out this work [43].

*james.thomas@materials.ox.ac.uk

[1] A. Mitra, I. Aleiner, and A. J. Millis, Phys. Rev. B **69**, 245302 (2004).
[2] H. Park, J. Park, A. K. L. Lim, E. H. Anderson, A. P. Alivisatos, and P. L. McEuen, Nature (London) **407**, 57 (2000).
[3] S. Sapmaz, P. Jarillo-Herrero, Y. M. Blanter, C. Dekker, and H. S. J. van der Zant, Phys. Rev. Lett. **96**, 026801 (2006).
[4] R. Härtle, M. Butzin, O. Rubio-Pons, and M. Thoss, Phys. Rev. Lett. **107**, 046802 (2011).
[5] E. Burzurí, Y. Yamamoto, M. Warnock, X. Zhong, K. Park, A. Cornia, and H. S. J. van der Zant, Nano Lett. **14**, 3191 (2014).
[6] C. S. Lau, H. Sadeghi, G. Rogers, S. Sangtarash, P. Dallas, K. Porfyrakis, J. Warner, C. J. Lambert, G. A. D. Briggs, and J. A. Mol, Nano Lett. **16**, 170 (2016).
[7] M. Galperin, M. A. Ratner, and A. Nitzan, J. Phys. Condens. Matter **19**, 103201 (2007).
[8] R. Leturcq, C. Stampfer, K. Inderbitzin, L. Durrer, C. Hierold, E. Mariani, M. G. Schultz, F. von Oppen, and K. Ensslin, Nat. Phys. **5**, 327 (2009).
[9] J. O. Thomas, B. Limburg, J. K. Sowa, K. Willick, J. Baugh, G. A. D. Briggs, E. M. Gauger, H. L. Anderson, and J. A. Mol, Nat. Commun. **10**, 4628 (2019).
[10] S. Braig and K. Flensberg, Phys. Rev. B **68**, 205324 (2003).
[11] J. K. Sowa, J. A. Mol, G. A. D. Briggs, and E. M. Gauger, J. Chem. Phys. **149**, 154112 (2018).
[12] J. E. Moser and M. Grätzel, Chem. Phys. **176**, 493 (1993).
[13] C. Zimmermann, F. Willig, S. Ramakrishna, B. Burfeindt, B. Pettinger, R. Eichberger, and W. Storck, J. Phys. Chem. B **105**, 9245 (2001).
[14] A. A. Bakulin, R. Lovrincic, X. Yu, O. Selig, H. J. Bakker, Y. L. Rezus, P. K. Nayak, A. Fonari, V. Coropceanu, J.-L. Brédas, and D. Cahen, Nat. Commun. **6**, 7880 (2015).
[15] S. Rafiq, B. Fu, B. Kudisch, and G. D. Scholes, Nat. Chem. **13**, 70 (2021).
[16] Z. Ioffe, T. Shamai, A. Ophir, G. Noy, I. Yutsis, K. Kfir, O. Cheshnovsky, and Y. Selzer, Nat. Nanotechnol. **3**, 727 (2008).
[17] D. R. Ward, D. A. Corley, J. M. Tour, and D. Natelson, Nat. Nanotechnol. **6**, 33 (2011).
[18] Y. Ke, A. Erpenbeck, U. Peskin, and M. Thoss, J. Chem. Phys. **154**, 234702 (2021).
[19] M. C. Luffe, J. Koch, and F. von Oppen, Phys. Rev. B **77**, 125306 (2008).
[20] R. Gaudenzi, M. Misiorny, E. Burzurí, M. R. Wegewijs, and H. S. J. van der Zant, J. Chem. Phys. **146**, 092330 (2017).
[21] J. Koch and F. von Oppen, Phys. Rev. Lett. **94**, 206804 (2005).
[22] J. Koch and F. von Oppen, Phys. Rev. B **72**, 113308 (2005).

[23] M. Leijnse and M. R. Wegewijs, Phys. Rev. B **78**, 235424 (2008).
[24] A. K. Huttel, B. Witkamp, M. Leijnse, M. R. Wegewijs, and H. S. J. van der Zant, Phys. Rev. Lett. **102**, 225501 (2009).
[25] C. S. Lau, J. A. Mol, J. H. Warner, and G. A. D. Briggs, Phys. Chem. Chem. Phys. **16**, 20398 (2014).
[26] S. Richert, B. Limburg, H. L. Anderson, and C. R. Timmel, J. Am. Chem. Soc. **139**, 12003 (2017).
[27] B. Limburg, J. O. Thomas, G. Holloway, H. Sadeghi, S. Sangtarash, I. C.-Y. Hou, J. Cremers, A. Narita, K. Müllen, C. J. Lambert, J. A. Mol, and H. L. Anderson, Adv. Funct. Mater. **28**, 1803629 (2018).
[28] See Supplemental Material at http://link.aps.org/supplemental/10.1103/PhysRevLett.129.207702 for synthetic details, additional transport and fitting data. All files related to a published paper are stored as a single deposit and assigned a Supplemental Material. This URL appears in the article's reference list.
[29] S. Ryu, L. Liu, S. Berciaud, Y.-J. Yu, H. Liu, P. Kim, G. W. Flynn, and L. E. Brus, Nano Lett. **10**, 4944 (2010).
[30] B. Limburg, J. O. Thomas, J. K. Sowa, K. Willick, J. Baugh, E. M. Gauger, G. A. D. Briggs, J. A. Mol, and H. L. Anderson, Nanoscale **11**, 14820 (2019).
[31] J. O. Thomas, J. K. Sowa, B. Limburg, X. Bian, C. Evangeli, J. L. Swett, S. Tewari, J. Baugh, G. C. Schatz, G. A. D. Briggs, H. L. Anderson, and J. A. Mol, Chem. Sci. **12**, 11121 (2021).
[32] J. Koch, F. von Oppen, and A. V. Andreev, Phys. Rev. B **74**, 205438 (2006).
[33] M. J. Frisch, G. W. Trucks, H. B. Schlegel, G. E. Scuseria, M. A. Robb, J. R. Cheeseman, G. Scalmani, V. Barone, G. A. Petersson, H. Nakatsuji *et al.*, Gaussian16 Revision C.01 (2016), Gaussian Inc., Wallingford CT.
[34] J. S. Seldenthuis, H. S. J. van der Zant, M. A. Ratner, and J. M. Thijssen, ACS Nano **2**, 1445 (2008).
[35] A. Pasupathy, J. Park, C. Chang, A. Soldatov, S. Lebedkin, R. Bialczak, J. Grose, L. Donev, J. Sethna, D. Ralph, and P. L. McEuen, Nano Lett. **5**, 203 (2005).
[36] K. J. Franke and J. I. Pascual, J. Phys. Condens. Matter **24**, 394002 (2012).
[37] A. Nitzan and J. Jortner, Mol. Phys. **25**, 713 (1973).
[38] H. Bi, C.-A. Palma, Y. Gong, K. Stallhofer, M. Nuber, C. Jing, F. Meggendorfer, S. Wen, C. Yam, R. Kienberger, M. Elbing, M. Mayor, H. Iglev, J. V. Barth, and J. Reichert, J. Am. Chem. Soc. **142**, 3384 (2020).
[39] A. Laubereau, D. von der Linde, and W. Kaiser, Phys. Rev. Lett. **28**, 1162 (1972).
[40] B. J. LeRoy, S. Lemay, J. Kong, and C. Dekker, Nature (London) **432**, 371 (2004).
[41] G. Bethardy, X. Wang, and D. S. Perry, Can. J. Chem. **72**, 652 (1994).
[42] D. Sun, W. Zhao, Q. Dai, F. Qiu, L. Ma, and G. Tian, Phys. Rev. B **104**, 245411 (2021).
[43] A. Richards, University of Oxford Advanced Research Computing, http://dx.doi.org/10.5281/zenodo.22558.